# Nanoscale

Accepted Manuscript


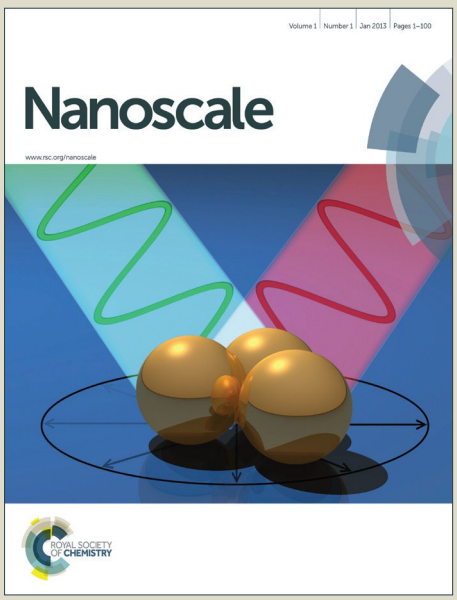





ROYAL SOCIETY OF CHEMISTRY

www.rsc.org/nanoscale

Journal Name

COMMUNICATION

# Synthesis of porous NiO/$CeO_2$ hybrid nanoflake arrays as platform for electrochemical biosensing

Received 00th January 20xx,
Accepted 00th January 20xx

DOI: 10.1039/x0xx00000x

www.rsc.org/

**Jiewu Cui*[a,b], Jinbao Luo[a], Bangguo Peng[a,b], Xinyi Zhang*[b], Yong Zhang[a,b], Yan Wang[a,b], Yongqiang Qin[a], Hongmei Zheng[a], Xia Shu[a,b] and Yucheng Wu*[a,b]**

**Porous NiO/$CeO_2$ hybrid nanoflake arrays fabricated by a facile hydrothermal method were employed as substrate for electrochemical biosensors. The resulting NiO/$CeO_2$ hybrid nanoflake arrays with large specific surface area and good biocompatibility presented an excellent platform for electrochemical biosensing.**

Over the past two decades, considerable interests have been devoted to the development of alternative nanomateirals as substrates for the construction of electrochemical biosensors, which are extensively employed to detect the concentration of glucose, cholesterol, dopamine etc. in the field of food quality analysis and clinical diagnosis[1-3]. Among various nanomaterials, different noble metal nanomaterials, such as Au, Pt, Pd, etc. were employed to construct biosensors, which presented high sensitivities towards relevant analytes[4-10]. In addition, different alloy nanomaterials were synthesized and used as substrates for biosensors to further improve the performance of biosensors due to the synergistic effects of different components[11-15]. However, the high cost and poor selectivity of noble nanomaterials-based biosensors impeded the practical applications of biosensors. In order to solve this problem, metal oxide nanomaterials, especially for nanomaterial arrays, have been investigated extensively to replace noble metal nanomaterials as electrochemical biosensing substrates due to their low cost, good selectivity, environmentally benign and excellent chemical stability[16-20]. In addition, metal oxide nanomaterials such as ZnO, $CeO_2$, NiO, $TiO_2$ and $Fe_3O_4$ exhibit different isoelectric point (IEP), which benefits the immobilization of different enzymes[21]. Especially for $CeO_2$ and NiO, their promising applications in the construction of biosensors have intrigued much research interest in the past half decade. Patil et al. have employed $CeO_2$ nanorods to fabricate glucose biosensor because of their excellent redox properties related to oxygen vacancy[19, 21]. Ali et al. have used NiO nanorods for application in cholesterol biosensing due to its high IEP (IEP: 10.8) and high electro-catalytic activities, which showed a high sensitivity of 120 $\mu A \cdot mM^{-1} \cdot cm^{-2}$ towards cholesterol determination[22]. Despite the considerable progress, the exploration of novel nanomaterials is still the most important step in development of metal oxide-based electrochemical biosensing substrates[23-26].

As aforementioned, the synergistic effect of different nanomaterials favours the improvement of performance of hybrid nanomaterial-based biosensors. Therefore, various hybrid metal oxide nanomaterials have been utilized as substrates for the construction of electrochemical biosensors[27-30]. In addition, ordered nanoarrays are helpful for the fabrication of biosensors with good reproducibility. In this communication, for the first time, we report a facile approach for the fabrication of porous NiO/$CeO_2$ hybrid nanoflake arrays and their applications in electrochemical biosensors. A novel nanomaterial, NiO/$CeO_2$ hybrid nanoflake arrays, is developed and employed as the substrate for the construction of glucose biosensors.

Fig. 1 (a), (b) and (c) show the SEM images of as-prepared samples on Ni foam after calcinations at 500 ℃ for 2 h with different magnifications. It is obvious that the Ni foam is completely covered by as-prepared samples with large scale as shown in Fig. 1 (a). Porous nanoflake arrays can be observed in Fig. (b) and (c), the thickness of porous nanoflake is about 10 nm and the pore size in the nanoflake is between 5 and 40 nm. The formation mechanism of porosity in the nanoflake arrays will be discussed later. X-ray diffraction technique is employed to characterize the phase structure of as-prepared nanoflake arrays before and after calcinations as demonstrated in Fig. 1(c), XRD pattern of nanoflake arrays before calcinations exhibits diffraction peaks of $Ce(OH)_3$ (JCPDS 19-0284) and $Ni(OH)_2$ (JCPDS 14-0117), and the diffraction peaks of samples after calcinations in Fig. 1(d) can be assigned to $CeO_2$ phase (JCPDS 34-0394) and NiO phase (JCPDS 47-1049), indicating

[a] *School of Materials Science and Engineering, Hefei University of Technology, Hefei,230009, China. Fax: +86 551-62904517; Tel: +86 551 62901012; E-mail: ycwu@hfut.edu.cn.*
[b] *Key Laboratory of Advanced Functional Materials and Devices of Anhui Province, Hefei, 230009, China.*

Electronic Supplementary Information (ESI) available: [Optical photograph of as prepared samples, SEM, TEM, EDS, XRD and BET data of the samples are presented, I-t curves of glucose biosensors based on NiO and NiO/$CeO_2$ NFAs, EIS results of different electrodes are shown here ]. See DOI: 10.1039/x0xx00000x

Journal Name

COMMUNICATION

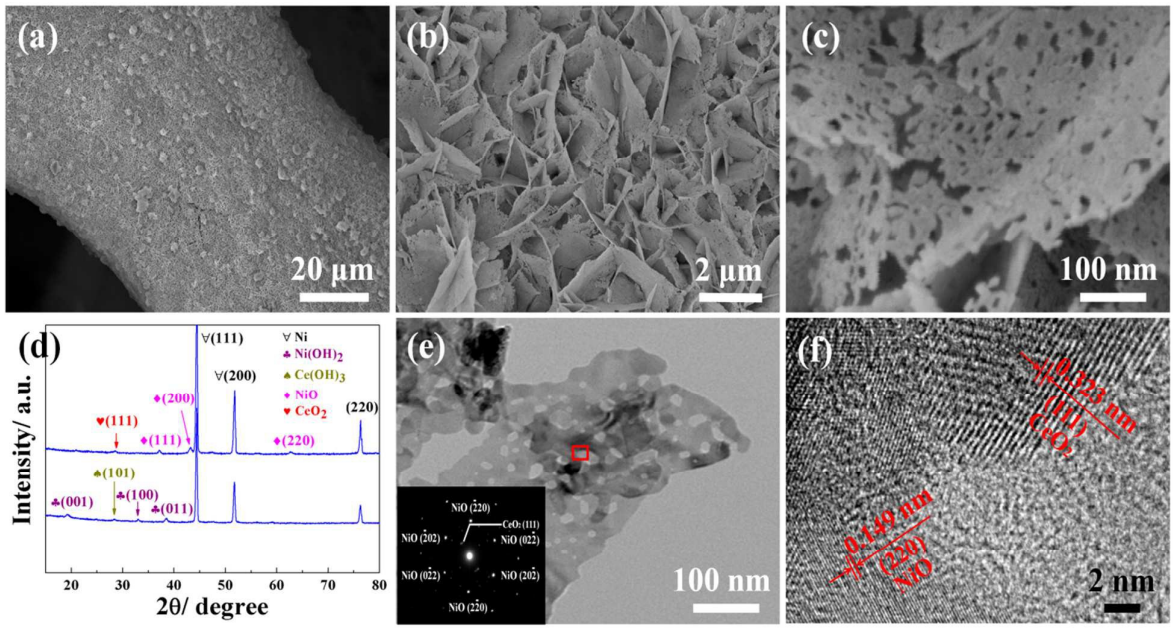


Fig.1 (a), (b) and (c) are SEM image of porous $NiO/CeO_2$ hybrid NFAs on Ni foam at different magnifications.(d) XRD patterns of as-prepared samples on Ni foam before and after calcinations. (e) TEM images of an individual porous $NiO/CeO_2$ hybrid nanoflake, Inset in Fig.1 (e) is SAED of corresponding porous $NiO/CeO_2$ hybrid nanoflake. (f) HRTEM image of $NiO/CeO_2$ hybrid nanoflake marked in Fig. 1(e).

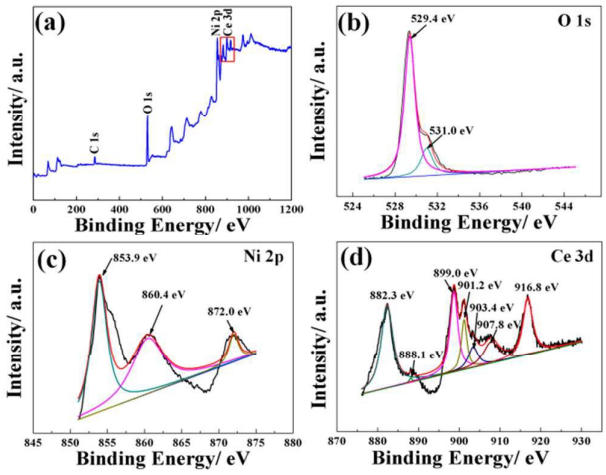


Fig.2 (a) XPS survey spectra of porous $NiO/CeO_2$ hybrid NFAs, (b) O 1s, (c) Ni 2p and (d) Ce 3d spectra of porous $NiO/CeO_2$ hybrid NFAs.

the formation of $NiO/CeO_2$ hybrid NFAs. In addition, the microstructure of an individual $NiO/CeO_2$ hybrid nanoflake is investigated in detail by TEM, SAED and HRTEM, respectively. Individual $NiO/CeO_2$ hybrid nanoflake shows porous structure and the pore size in the $NiO/CeO_2$ hybrid nanoflake is between 5 and 40 nm, which is in good agreement with the SEM result in Fig. 1(c). And SAED pattern of $NiO/CeO_2$ hybrid nanoflake shows the nanoflake is single crystal, which is presented in Inset in Fig. 1(e). Fig. 1(f) exhibits the HRTEM image of the $NiO/CeO_2$ hybrid nanoflake are indicated in Fig. 1(e). The lattice fringes with a lattice spacings of about 0.149 nm and 0.323 nm correspond to the (220) plane of NiO and the (111) plane of $CeO_2$, respectively, which also suggests the co-existence of NiO phase and $CeO_2$ phase. In addition, the BET surface area of as-prepared samples is calculated to be 55.9 $m^2 \cdot g^{-1}$ according to nitrogen adsorption and desorption isotherm as shown in Fig.S1.

XPS analysis is further employed to investigate the chemical bonding states of as-prepared samples and the results are presented in Fig. 2. Ce species is clearly detected in the porous $NiO/CeO_2$ hybrid NFAs as shown in Fig. 2(a). The O 1s spectrum in Fig.2(b) exhibits two peaks centered at 529.4 eV and 531.0 eV, respectively, which may originate from the oxygen species of metal-oxide in the NFAs and adsorbed $OH^-$ species on the surface of the NFAs[31]. Furthermore, the oxidation states of Ni and Ce are also confirmed by Ni 2p and

Ce 3d XPS spectra. Fig.2(c) shows peaks centered at 853.9 eV and 872.0 eV, which are two main Ni $2p_{3/2}$ and Ni $2p_{1/2}$ peaks, respectively. In addition, there is a shake-up satellite peak centered at 864.0 eV, fitting with the binding states of NiO[32]. Fig. 2(d) demonstrates the Ce 3d spectrum, the peaks centered at 882.3 eV, 888.1 eV, and 899.0 eV belong to Ce $3d_{5/2}$, and peaks at 901.2 eV, 903.4 eV, 907.8 eV and 916.8 eV correspond to Ce $3d_{3/2}$. Only the peak centered at 903.4 eV belongs to $Ce^{3+}$, and the other peaks are ascribed to $Ce^{4+}$.[33-35] The XPS analysis is consistent with the SAED and HRTEM results in Fig. 1(e) and (f).

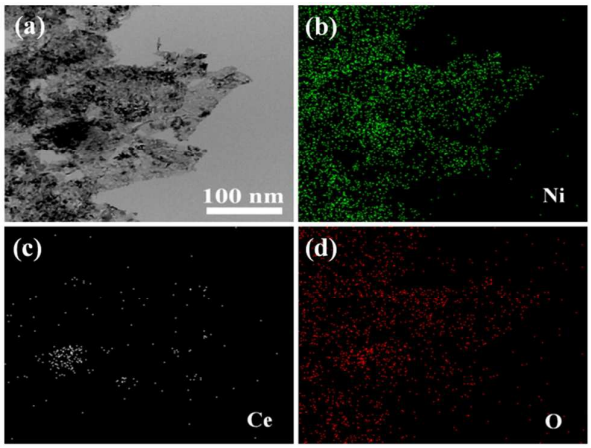


Fig. 3 (b-d) EDX mapping of (a) porous $NiO/CeO_2$ hybrid NF.

The composition distribution in the hybrid nanoflake is characterized by the energy dispersive X-ray spectroscopy (EDX), and the results are demonstrated in Fig. 3. Ni, Ce and O elements distribute uniformly in hybrid nanoflake, and the amount of Ce element is obviously less than that of Ni. This is in consistence with the EDS analysis results. The EDS result indicates that the atomic ratio of Ni and Ce is about 5.9, as shown in Fig. S2 and Table S1. In order to understand the formation mechanism of the porous $NiO/CeO_2$ hybrid NFAs, a control experiment is carried out as follows: Nickel foam is hydrothermal treated in mixture solution without $Ce(NO_3)_3$ and then calcinated at 500℃ for 2h. Subsequently, porous NiO NFAs are synthesized and confirmed in Fig. S3.

The main chemical reactions involved in hydrothermal process and calcinations can be summarized as follows:

$$CO(NH_2)_2 + H_2O \rightarrow 2NH_3 + CO_2 \quad (1)$$

$$CO_2 + H_2O \rightarrow CO_3^{2-} + 2H^+ \quad (2)$$

$$NH_3 \cdot H_2O \rightarrow NH_4^+ + OH^- \quad (3)$$

$$Ni + 2H^+ \rightarrow Ni^{2+} + H_2 \quad (4)$$

$$Ni^{2+} + xF^- \rightarrow [NiF_x]^{(x-2)-} \quad (5)$$

$$Ce^{3+} + xF^- \rightarrow [CeF_x]^{(x-3)-} \quad (6)$$

$$[NiF_x]^{(x-2)-} + 2OH^- \rightarrow Ni(OH)_2 + xF^- \quad (7)$$

$$[CeF_x]^{(x-3)-} + OH^- + Ni(OH)_2 \rightarrow Ce(OH)_3 + [NiF_x]^{(x-2)-} \quad (8)$$

$$Ni(OH)_2 \rightarrow 2NiO + H_2O \quad (9)$$

$$4Ce(OH)_3 + O_2 \rightarrow 4CeO_2 + 6H_2O \quad (10)$$

Taking the aforementioned results into account, when nickel foam is immersed into the mixture solution, nickel on the surface of Ni foam is etched away by $H^+$ according to equation (2) and $Ni^{2+}$ forms in the mixture solution. Subsequently, $Ni(OH)_2$ is formed in the hydrothermal process as shown in equation (7). Interestingly, $Ce^{3+}$ ions can't form $Ce(OH)_3$ directly with $OH^-$ without nickel foam substrate, which is confirmed by the results presented in Fig. S4. However, $Ce(OH)_3$ is detected when nickel foam is put into the mixture solution as shown in Fig. 1(d), the possible mechanism for formation of $Ce(OH)_3$ is inferred to be the cation exchange between $Ce^{3+}$ and $Ni^{2+}$ in $Ni(OH)_2$, resulting in the colour change of mixture solution before and after hydrothermal reaction as shown in Fig. S5(b). Therefore, the $Ni(OH)_2/Ce(OH)_3$ hybrid NFAs precursors are synthesized and further confirmed by HRTEM result in Fig. S6. In addition, as-prepared $Ni(OH)_2/Ce(OH)_3$ hybrid NFAs are smooth without porous structure (Fig. S6 (a) and (b)). $Ni(OH)_2/Ce(OH)_3$ hybrid NFAs are converted into $NiO/CeO_2$ hybrid NFAs during calcinations at 500 ℃ according to equations (9) and (10). Meanwhile, the weight loss and volume shrinking because of the release of $H_2O$ in the calcinations process create the porous feature of $NiO/CeO_2$ hybrid NFAs, which is analogous to formation mechanism of the porous nanostructures previously reported. It is worth noting that the cation exchange between $Ce^{3+}$ and $Ni^{2+}$ in $Ni(OH)_2$ is not only in favour of formation of $Ni(OH)_2/Ce(OH)_3$ hybrid NFAs, but also promotes the growth of $Ni(OH)_2/Ce(OH)_3$ hybrid nanoflake, which can be easily observed in Fig. S7(a) and (b). When $Ce(NO_3)_3$ is added into the mixture solution, the size of $NiO/CeO_2$ nanoflake is undoubtedly larger than that of phase-pure NiO nanoflake. Furthermore, the thickness of $NiO/CeO_2$ nanoflake increases with increasing $Ce(NO_3)_3$ concentration as demonstrated in Fig. S7. However, once the concentration of $Ce(NO_3)_3$ is higher than 20 mM, excess $Ce^{3+}$ reacts with $F^-$ from $NH_4F$ to form $CeF_3$, resulting in a great amount of unfixed $CeF_3$ nanoparticles on the surface of $NiO/CeO_2$ nanoflakes(Fig. S8). In addition, the influences of hydrothermal temperature, hydrothermal time, $NH_4F$ and $CO(NH)_2$ concentrations on the morphology of $NiO/CeO_2$ NFAs are investigated systematically and the results are depicted in Fig. S9-12.

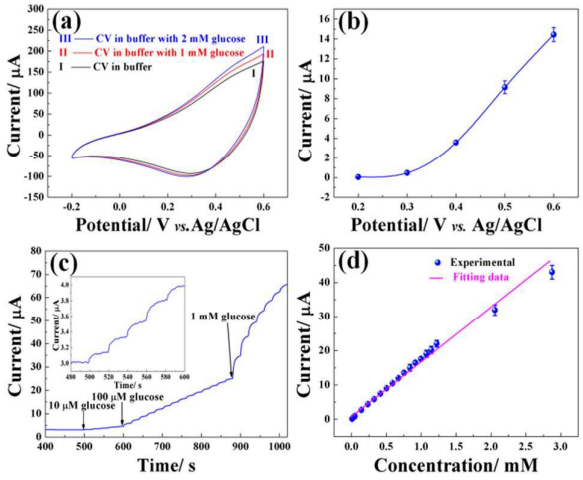


Fig. 4 (a) Cyclic voltammograms of $NiO/CeO_2$ hybrid NFAs-based glucose biosensors in 0.05 M PBS with different glucose concentrations. (b) Working potential optimization. (c) I-t curve of $NiO/CeO_2$ hybrid NFAs-based glucose biosensor with successive injection of different concentration of glucose, Inset is the I-t curve of $NiO/CeO_2$ hybrid NFAs-based glucose biosensors with successive injection of 10 μM glucose. (d) Calibration curve of as-prepared glucose biosensor.

As-prepared $NiO/CeO_2$ hybrid NFAs are used for substrate to construct biosensor and glucose is selected as the target to validate the performance of $NiO/CeO_2$ hybrid NFAs. Although porous $NiO/CeO_2$ hybrid NFAs also have high excellent activity towards glucose due to the $Ni^{2+}/Ni^{3+}(Ce^{3+}/Ce^{4+})$ couples, however, the catalytic performance of $NiO/CeO_2$ hybrid NFAs towards glucose can only take place in alkaline solution, which needs enough $OH^-$ anions. But this can not happen in mild phosphate buffer solution due to lack of $OH^-$[36, 37]. In addition, experimental results show that the selectivity of non-enzymatic glucose sensor in alkaline solution is worse than that of enzymatically-based glucose biosensor in PBS as shown in Fig. S13 and Fig. S17. Although the sensitivity of non-enzymatic glucose sensor is high, the poor selectivity impedes the practical applications in the detection of glucose. Fig. S14 shows the SEM images of $NiO/CeO_2$ hybrid NFAs after modification by cross linking approach, in which $NiO/CeO_2$ hybrid NFs are apparently covered by a thin film, indicating the successful immobilization of glucose oxidase. The electrochemical performance of glucose biosensors based on $NiO/CeO_2$ hybrid NFAs is investigated by cyclic voltammogram (CV) and chronoamperometry, respectively. Fig. 4 (a) depicts the cyclic voltammograms of glucose biosensors based on $NiO/CeO_2$ hybrid NFAs in phosphate buffer solution with different glucose concentrations. The results suggest that the current increases with increasing of glucose concentrations and working potential, and subsequently the influence of working potential on amperometric response of glucose biosensor is further investigated as shown in Fig. 4(b). The amperometric response increase with the increase of working potential from 0.3 V to 0.6 V, which is in good agreement with the CV results in Fig. 4(a). Eventually, working potential of 0.6 V is selected and utilized in the following experiments. In addition, glucose biosensor based on NiO NFAs is also constructed and the amperometric responses of glucose biosensors based on different substrates are measured under the same condition and compared. Glucose biosensor based on $NiO/CeO_2$ hybrid NFAs exhibits higher amperometric responses than that of glucose biosensor based on NiO NFAs (Fig. S15), demonstrating $NiO/CeO_2$ hybrid NFAs being excellent substrate for the construction of biosensors. The sensing mechanism of glucose biosensors based on $NiO/CeO_2$ hybrid nanoflake arrays is as follows: glucose will be enzymatically catalyzed to gluconic acid and $H_2O_2$ when glucose reaches active sites of glucose oxidase. And $H_2O_2$ transfers to the surface of $NiO/CeO_2$ NFAs, where it is oxidized to $O_2$ by NiO and $CeO_2$ and gives ameprometric responses. The amperometric responses are eventually proportional to the concentration of glucose. On the one hand, both NiO and $CeO_2$ exhibit catalytic performance towards $H_2O_2$ produced in the enzymatically catalyzed reactions by glucose oxidase; on the other hand, the hybridization of NiO and $CeO_2$ decreases charge transfer resistance of as-prepared samples(Fig. S16 and Table S2), which favours the electron transfer during enzymatically catalyzed reactions. Fig. 4 (c) shows typical amperometric response of glucose biosensor based on $NiO/CeO_2$ hybrid NFAs with successive injection of various concentrations of glucose, the current increases with the successive injection of glucose. The sensitivity of glucose biosensor based on $NiO/CeO_2$ hybrid NFAs is 154.4 $\mu A \cdot cm^{-2} \cdot mM^{-1}$, which is much higher than those of glucose biosensors based on other metal oxide nanostructures reported previously, such as ZnO nanofiber(70.2 $\mu A \cdot cm^{-2} \cdot mM^{-1}$), $MnO_2$ nanoparticle(24.2 $\mu A \cdot cm^{-2} \cdot mM^{-1}$), NiO film (101.8 $\mu A \cdot cm^{-2} \cdot mM^{-1}$) and NiO/ZnO nanorods (61.78 $\mu A \cdot cm^{-2} \cdot mM^{-1}$) [16-19,38,39] The linear range between 1.0 and 2,900 μM ($R^2$=0.99) is obtained for the glucose biosensor as shown in Fig. 4(d) and the minimum detectable glucose concentration of 1.0 μM is employed as the detection limit. And the comparison of glucose biosensors based on the $NiO/CeO_2$ hybrid NWAs and other representative nanomaterials is given in Table S3. In addition, glucose biosensor based on $NiO/CeO_2$ hybrid NFAs demonstrates excellent selectivity towards interferences co-existence with glucose(Fig. S17), which also indicates $NiO/CeO_2$ hybrid NFAs are superb substrate for electrochemical biosensing.

## Conclusions

In summary, porous $NiO/CeO_2$ hybrid NFAs are fabricated by a hydrothermal procedure on Ni foam. The as-prepared porous $NiO/CeO_2$ hybrid NFAs are utilized to construct amperometric glucose biosensor and it exhibits excellent performance, such as high sensitivity, low detection limit and wide linear range. It is believed that this novel $NiO/CeO_2$ hybrid NFAs is an excellent substrate which can be extended to fabricate other oxidase-based biosensors, such as cholesterol biosensors, etc.

## Acknowledgements

This work is financially supported by National Natural Science Foundation of China (Grant Nos. 51272063 and 51402081), National Key Fundamental Research Development Program (Grant No. 2014CB660815). Natural Science Foundation of Anhui Province (Grant No. 1408085QB42) is also gratefully appreciated.

## Notes and references

1 J. Wang, Chem. Rev., 2008, 108, 814.
2 Y. J. Song, K. G. Qu, C. Zhao, J. S. Ren, X. G. Qu, Adv. Mater., 2010, 22, 2206.
3 E. Asav, E. Akyilmaz, Biosens. Bioelectron., 2010, 25, 1014.
4 M. H. Yang, F. L. Qu, Y. S. Lu, Y. He, G. L. Shen, R. Q. Yu, Biomater., 2006, 27, 5944.
5 Y. L. Wang, Y. C. Zhu, J. J. Chen, Y. Zen,Nanoscale, 2012, 4, 6025.
6 J. W. Cui, S. B. Adeloju, Y. C. Wu, Anal. Chim. Acta,2014, 809,134.
7 D. Wen, S. J. Guo, S. J. Dong, E. K. Wang, Biosens. Bioelectron.,2010, 26, 1056.
8 X. J. Yang, J. Bai, Y. H. Wang, X. Jiang, X. Y. He, Analyst, 2012, 137, 4362.
9 X. Y. Zhang, D. Li, L. Bourgeois, H. T. Wang, P. A. Webley, ChemPhysChem, 2009,10, 436.
10 F. Wang, X. Q. Liu,C. H. Lu,I. Willner,ACS Nano,2013, 7, 7278.
11 S. Q. Wang, L. P. Xu, H. W. Liang, S. H. Yu, Y. Q. Wen, S. T. Wang, X. J. Zhang,Nanoscale, 2015, 7, 11460.
12 M. Hamal, J. Xu, K. M. Razeeb, Biosens. Bioelectron.,2010, 26, 1420.
13 J. W. Cui, E. E. Ogabiela, J. N. Hui, Y. Wang, Y. Zhang, L. Tong, J. F. Zhang, S. B. Adeloju, X. Y. Zhang, Y. C. Wu, J. Electrochem. Soc., 2015, 162, B62.
14 N. Moghimi, K. T. Leung, Anal. Chem., 2013, 85, 5974.
15 J. Yang, S. Y. Deng, J. P. Lei, H. X. Ju, S. Gunasekaran, Biosens. Bioelectron., 2011, 29, 159.
16 Y. Zhang, Z. Kang, X. Q. Yan, Q. L. Liao, Sci China Mater., 2015,58,60.
17 M. Ahmad, C. F. Pan, Z. X. Luo, J. Zhu, J. Phys. Chem. C, 2010, 114, 9308.
18 J. Singh, P. Kalita, M. K. Singh, B. D. Mahotra, Appl. Phys. Lett., 2011, 98, 123702.
19 D. Patil, N. Q. Dung, H. Jung, S. Y. Ahn, D. M. Jang, D. Kim, Biosens. Bioelectron., 2012, 31, 176.
20 S. J. Bao, C. M. Li,J. F. Zang, X. Q. Cui, Y. Qiao, J. Guo, Adv. Funct. Mater.,2008, 18, 591.

21 D. S. Zhang, X. J. Du, L. Y. Shi, R. H. Gao, Dalton Trans., 2012, 41, 14455.
22 M. A. Ali, P. R. Solanki, M. K. Patel, H. Dhayani,V. V. Agrawal, R. John, B. D. Malhotra, Nanoscale, 2013, 5, 2883.
23 K. Arora, M. Tomar, V. Gupta,2014, 139, 4606.
24 A. K. Yagati, T. Lee, J. Min, J. W. Choi, Biosens. Bioelectron., 2013, 47, 385.
25 Y. B. Hahn, R. Ahmada, N. Tripathy, Chem. Commun., 2012, 48, 10369.
26 P. R. Solanki, A. Kaushik, V. V. Agrawal, B. D. Malhotra, NPG Asia Mater., 2011, 3, 17.
27 J. Njagi, C. Ispas, S. Andreescu, Anal. Chem., 2008, 80, 7266.
28 J. M. Yang, W. Zhang, Q. Liu, W. Y. Sun, RSC Adv., 2014, 4, 51098.
29 R. E. Özel, C. Ispas, M. Ganesana, J. C. Leiter, S. Andreescu, Biosens. Bioelectron.,2014, 52, 397.
30 J. W. Zhao, F. Mu, L. R. Qin, X. Y. Jia, C. F. Yang, Mater. Chem. Phys., 2015, 166, 176.
31 D. W. Wang, Q. H. Wang, T. M. Wang, Inorg. Chem., 2011,50, 6482.
32 G. F. Cai, J. P. Tu, J. Zhang, Y. J., Mai, Y. Lu, C. D., Gu, X. L. Wang, Nanoscale, 2012, 4, 5724.
33 T. Wang, L. D. Zhang, J. X. Zhang, G. M. Hua, Micropor. Mesopor. Mater., 2013, 171, 196.
34 C. Zhang, X. Y. Zhang, Y. C. Wang, S. L. Xie, Y. Liu, X. H. Lu, Y. X. Tong, New J. Chem., 2014, 38, 2581-2586.
35 J. W. Cui, X. Y. Zhang, L. Tong, J. B. Luo, Y. Wang, Y. Zhang, K. Xie, Y. C. Wu, J. Mater. Chem. A, 2015, 3, 10425.
36 Y. Ding, Y. Wang, L. Su, H. Zhang, Y. Lei, J. Mater. Chem., 2010, 20, 9918.
37 G. M. Wang, X. H. Lu, T. Zhai, Y. C. Ling, H. Y. Wang, Y. X. Tong, Y. Li, Nanoscale, 2012, 4, 3123.
38 J. J. Yu, T. Zhao, B. Z. Zeng, Electrochem. Commun., 2008, 10, 1318.
39 X. F. Chu, X. H. Zhu, Y. P. Dong, T. Y. Chen, M. F. Ye, W. Q. Sun, J. Electroanal. Chem., 676, 2012, 20.